NSU3D Results for the First AIAA High Lift Prediction Workshop

Mike Long [*]

Dimitri Mavriplis [†]

Department of Mechanical Engineering

University of Wyoming, Laramie, Wyoming, 82072-3295

Simulation results for the first AIAA CFD High Lift Prediction Workshop using the unstructured computational fluid dynamics code NSU3D are presented. The solution algorithms employed in NSU3D for this study are described along with examples of convergence history and computational cost. The geometry used for the simulation is the NASA three-element swept wing (Trap Wing) model with experimental data taken in the 14x22 foot wind tunnel at NASA Langley. Computational grids for the study were prepared by the authors with the VGRIDns package using CAD geometry provided by the workshop committee. A grid convergence study was performed using a family of three grids to assess sensitivity to grid resolution. A range of angle-of-attack values from $6°$ to $37°$ was completed on the medium grid and the resulting lift, drag and longitudinal moments are compared to the experimental results. The effect of changing the flap angle is investigated with a second model using an equivalent medium grid. Comparisons of surface pressure to experimental data are presented for both configurations. Flow features are also presented using surface constrained and volume streamlines for selected cases.

I. Introduction

Modeled on the successful Drag Prediction Workshop series, the High Lift Prediction Workshop Series was initiated under the sponsorship of the AIAA Applied Aerodynamics Technical Committee in 2009. The first Workshop was held during the 40th AIAA Fluid Dynamics Conference in Chicago IL in June 2010. The goals of the workshop are to assess the state-of-the-art in computational fluid dynamics (CFD) methods for simulation of high lift configurations and to provide a forum for exchange of ideas and practices related to this class of problem.

The geometry chosen for the workshop is the NASA trapezoidal wing (Trap Wing) that has been tested extensively in the 14x22 foot wind tunnel at NASA Langley Research Center. Figure 1 shows the Trap Wing model installed in the wind tunnel. The configuration consists of a three element wing with full span slat and flap with a 30 degree quarter-chord sweep, an aspect ratio of 4.56, and a taper ratio of 0.4. Two different flap deflections were studied, noted as Configuration 1 (25 degree flap deflection) and Configuration 8 (20 degree flap deflection). The mean aerodynamic chord of the model is 39.6 inches, and the wind tunnel experiments used for comparison in the workshop were carried out at a Reynolds number of 4.3 million, with no transition tripping mechanisms employed (i.e. free transition). Experimental results include forces and moments, as well as pressure measurements at over 700 surface locations and flow visualization in the form of surface mini-tufts. Further information about the geometry and wind tunnel tests is available in a number of studies.[1–3] The objective of this paper is to document the results for the first High Lift Prediction Workshop obtained using the NSU3D unstructured mesh Reynolds-averaged Navier-Stokes solver. The NSU3D code has been a participant in all four Drag Prediction workshops since 2001.[4–9] The NSU3D solver has also been involved in various DPW follow-on studies, including comparisons with other solvers,[10,11] sensitivity studies, and extensive grid refinement studies.[12,13]

---

[*]Applications Engineer, Member, email: mlong16@uwyo.edu

[†]Professor, Associate Fellow, email: mavripl@uwyo.edu

American Institute of Aeronautics and Astronautics

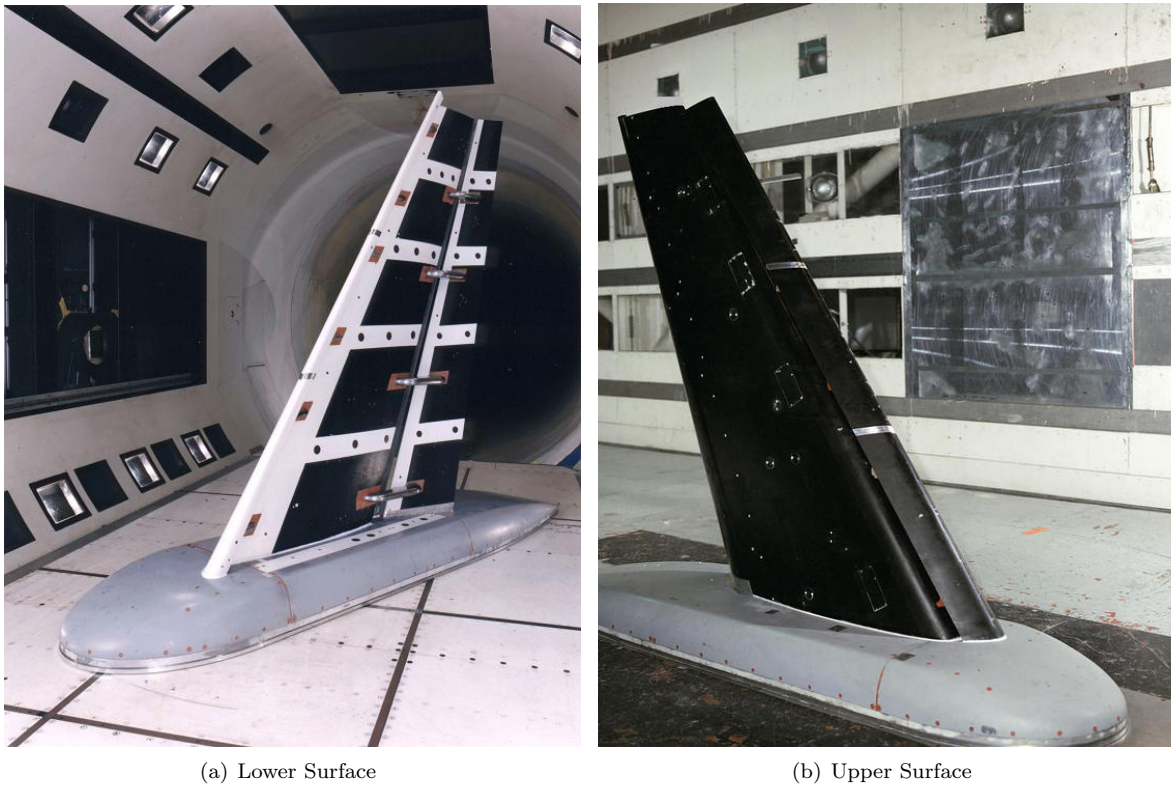(a) Lower Surface   (b) Upper Surface

Figure 1. NASA Trapezoidal Wing Wind Tunnel Model

The NSU3D solver is described briefly in the next section. In Section III an overview of the grids produced for the study is presented. Sections IV and V provide the results for the grid convergence study and the angle of attack sweeps for the two flap positions, respectively. Detailed comparison of surface pressures with experiment are presented in section VI. Flowfield visualization is then presented in Section VII followed by summary and conclusions in Section VIII.

II.   Solver Description

The NSU3D code is an unstructured mesh multigrid Reynolds-averaged Navier-Stokes (RANS) solver for high-Reynolds number external aerodynamic applications. The NSU3D discretization employs a vertex-based approach, where the unknown fluid and turbulence variables are stored at the vertices of the mesh, and fluxes are computed on faces delimiting dual control volumes, with each dual face being associated with a mesh edge. This discretization operates on hybrid mixed-element meshes, generally employing prismatic elements in highly stretched boundary layer regions, and tetrahedral elements in isotropic regions of the mesh away from the aircraft surfaces. A single edge-based data-structure is used to compute flux balances across all types of elements. The convective terms are discretized as central differences with added matrix dissipation. Second-order accuracy is achieved by formulating these dissipative terms as an undivided bi-harmonic operator, which is constructed in two passes of a nearest-neighbor Laplacian operator. In the matrix form, this dissipation is similar to that produced by a Riemann solver gradient-based reconstruction scheme, and is obtained by replacing the difference in the reconstructed states on each side of the control volume interface by the undivided differences along mesh edges resulting from the biharmonic operator construction. These differences are then multiplied by the characteristic matrix to obtain the final dissipation terms. A Roe upwind scheme using least-squares gradient reconstruction is also available in the NSU3D solver, although this option has not been used in the present study. Previous work has shown that the matrix dissipation and Roe schemes in NSU3D give very similar results, with the matrix dissipation scheme being slightly less diffusive overall.[9, 13]

The baseline NSU3D discretization employs a finite-difference scheme to approximate the thin-layer form

American Institute of Aeronautics and Astronautics

of the viscous terms for the Navier-Stokes equations, although this is done in a multidimensional fashion, by computing a Laplacian of the velocity field.[14] The main approximation in this approach is the omission of the cross-derivative viscous terms, and the assumption of a locally constant viscosity. The discretization of the full Navier-Stokes terms has also been implemented using a two-pass edge-based loop approach,[9] although this option has not been used in the present study.

NSU3D incorporates the single equation Spalart-Allmaras turbulence model,[15] as well as a standard $k-\omega$ two-equation turbulence model,[16] and the two-equation shear-stress transport (SST) model due to Menter.[17] Facilities for specified transition location based on the surface geometry are provided. While this capability was employed in DPW II,[5,11] the cases for the current study were all run fully turbulent in the absence of any given transition locations.

The basic time-stepping scheme in NSU3D consists of a three stage explicit multistage scheme. Convergence is accelerated by a local block-Jacobi preconditioner in regions of isotropic grid cells. In boundary layer regions, where the grid is highly stretched, a line preconditioner is employed to relieve the stiffness associated with the mesh anisotropy.[18] An agglomeration multigrid algorithm is used to further enhance convergence to steady-state.[14,19] The Jacobi and line preconditioners are used to drive the various levels of the multigrid sequence, resulting in a rapidly converging solution technique.

Figure 2 illustrates typical solution convergence seen on the coarse grid for the low angle of attack cases. Figure 3 shows an example of a higher angle of attack case on the fine grid. The large areas of separated and unsteady flow seen in these cases limited the ability of the solver to converge fully using the full multigrid algorithm. For these cases the solver is restarted without multigrid and then run for several thousand iterations to improve the solution convergence. As can be seen in the figure, the final lift value exhibits a small amount of oscillation, in this case approximately six counts of lift. For these cases, the lift is averaged over the last thousand iterations to arrive at the final value. Since the residual history is continuously decreasing in these cases, it has been verified that further solver iterations can be used to annihilate these remaining force coefficient variations. However, the resulting final force and moment values are virtually identical to those obtained through the above averaging process. Furthermore, although the force coefficients exhibited larger unsteady variations using the multigrid algorithm alone (i.e. first 2000 cycles) the average of these variations in most cases was also close to the final averaged single grid values and the fully converged values.

The collective workshop results revealed a possible hysteresis effect, requiring many participants to initialize high incidence cases with flow fields obtained at lower incidences to obtain suitably converged high incidence solutions.[20] In the current work, all NSU3D cases were initialized with freestream conditions. For Configuration 1, no dependence on initial conditions was observed. For Configuration 8, initial condition dependence was not observed, although the average forces obtained using multigrid alone were substantially different than the final values obtained after further single grid convergence. This is illustrated in the convergence history plot for Configuration 8 at 32 degrees incidence, depicted in Figure 4. After several thousand multigrid cycles, the residual convergence has stalled out, although the C_L values appear to be oscillating about a fixed mean. When the single grid solver is applied, residual convergence resumes while the C_L value migrates to a higher value which agrees more closely with the workshop collective results and the experimental data. This behavior of the multigrid algorithm at high alpha cases was not seen in the calculations performed on Configuration 1 (c.f. Figure 3) and was unexpected. Work is underway currently to enable more efficient multigrid convergence for high incidence cases.

NSU3D employs a dual level parallelization strategy invoking the MPI interface for interprocessor communication across distributed memory nodes, with the ability to use OpenMP constructs for inter-node shared memory parallelism. NSU3D has been shown to scale well on massively parallel computer architectures using up to 4000 cores.[21] The results reported in this paper have been run on the NASA Pleiades machine, using MPI exclusively and using from 32 to 256 cores. Typical wall clock requirements were approximately 1.5 hours for 1000 solver iterations on the medium grid using 64 cores.

III. Grid Generation

All of the grids used for this study were produced by the authors using the NASA Langley VGRIDns unstructured grid generator with the GridTool front end. Table 1 lists the node and cell counts for each grid. A total of four different grids were used for these calculations. Two configurations for the Trap Wing geometry were used to generate the grids. The first, referred to as Configuration 1 has the slat set to 30°
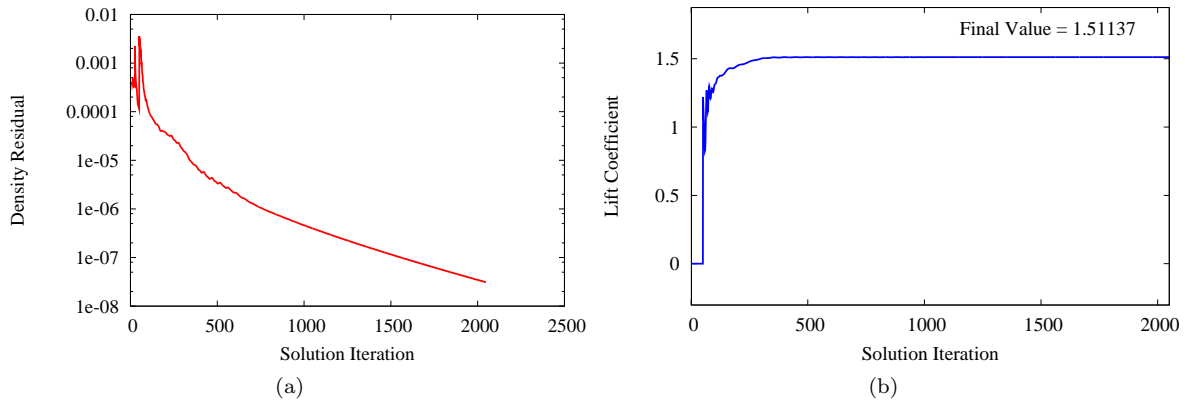
American Institute of Aeronautics and Astronautics

Figure 2. Typical convergence history for (a) density residual and (b) lift coefficient for lower incidence cases (Configuration 1 at 6 degrees incidence)
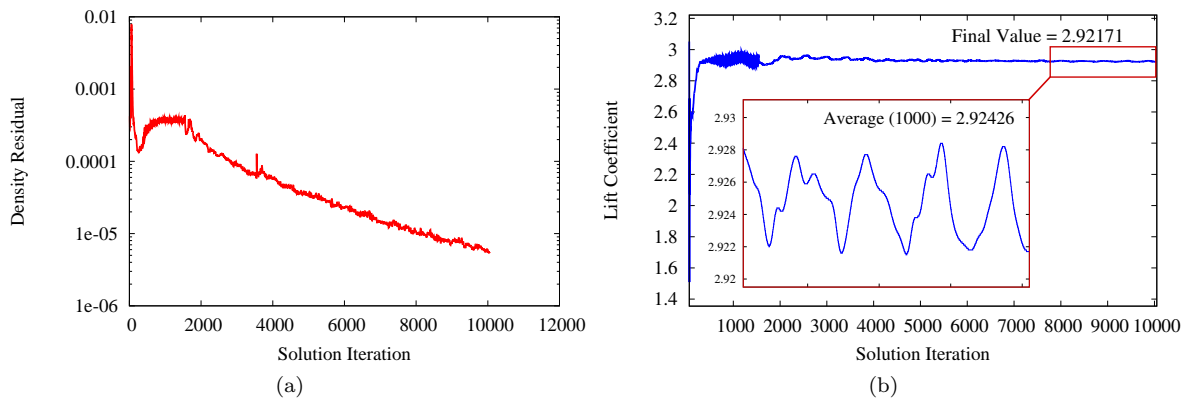

Figure 3. Convergence history for (a) density residual and (b) lift coefficient for Configuration 1 at 28 degrees incidence
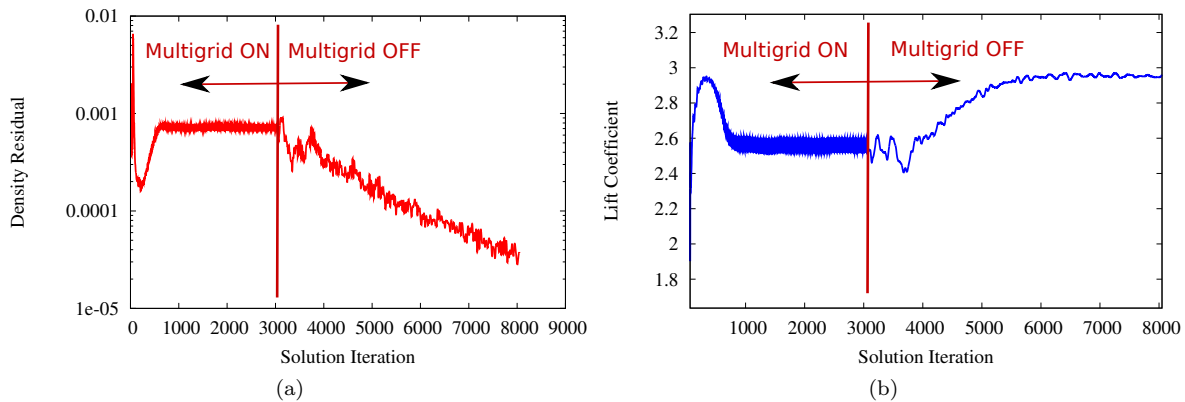

Figure 4. Convergence of (a) density residual and (b) lift coefficient for Configuration 8 at 32 degrees incidence illustrating resumption of residual convergence and higher lift produced with additional single grid solver iterations (multigrid off).

American Institute of Aeronautics and Astronautics

and the flap set to 25°. The second, referred to as Configuration 8 is identical to the first except that the flap angle is reduced to 20°. The CAD data for grid generation was supplied by the workshop committee in IGES format.

The grid refinement study was confined to Configuration 1 and required the generation of three progressively finer grids (referred to as coarse, medium and fine). A medium level resolution mesh was then generated for Configuration 8 with the grid generation parameters set to match what was used for Configuration 1 as closely as possible.

As was done for the drag prediction workshop series, a set of gridding guidelines has been produced and is summarized in Reference.[22] The meshing guidelines include a farfield boundary at 100 chord lengths away, a normal spacing at the wall of y+ $\leq$ 1.0 for the coarsest grids, with progressively smaller spacings on the finer grids, chordwise spacings at the element leading and trailing edges of approximately 0.1% chord on the coarse mesh, and spanwise spacings of 0.1% at the element root and tip on the coarsest mesh as well. A resolution of 4, 6, and 9 cells across the blunt trailing edge of the elements was specified for the coarse, medium and fine grids respectively, and the overall size of the grids was targeted to grow by a factor of three when going from coarse to medium, and medium to fine. Care was taken to generate corresponding coarse, medium and fine meshes with self-similar resolution distributions, such that these grids can be considered to be of the same "family" for grid convergence studies.[23] The medium grid was specified to be representative of the resolution level used in current industrial production runs. The final grids have been made available on the HLPW web site under the designation "Tet-Nodecentered-A-v1"[24] and have been used by various other workshop participants.[20]

NSU3D supports hybrid meshes with different element types and the preferred mode of operation is to employ prismatic elements in boundary layer regions. Therefore, the fully tetrahedral meshes generated by VGRIDns are transformed into hybrid prismatic-tetrahedral meshes in a preprocessing phase, by merging triplets of tetrahedra in the boundary layer regions into prismatic elements prior to NSU3D computations. This process also results in a small number of pyramidal elements in regions where exposed prismatic quadrilateral faces interface with tetrahedral elements. The final hybrid-element mesh characteristics are listed in Table 2.

Figure 5 shows the relative mesh resolution over the full model, while Figures 6 and 7 show the grid resolution in the flap cove and outboard slat regions, respectively.

Table 1. Descriptions of grids. Boundary layer spacings are in inches.

Grid Name	Nodes	Tetras	y+	BL Spacing	Notes
HLPW_WB-41AC	3652657	21492137	1.0	0.00020	Config 1, Coarse
HLPW_WB-41A	10957783	64441259	2/3	0.00013	Config 1, Medium
HLPW_WB-41AF	32297530	189895740	4/9	0.00009	Config 1, Fine
HLPW_WB-41A-8	11524779	67783972	2/3	0.00013	Config 8, Medium

Table 2. Descriptions grids after merging of boundary layer tetrahedra into prismatic elements for NSU3D

Grid Name	Nodes	Tetras	Prisms	Pyramids
HLPW_WB-41AC	3737533	4182361	5799630	167633
HLPW_WB-41A	11050263	24241228	13431459	184027
HLPW_WB-41AF	32453953	95172131	31627392	311774
HLPW_WB-41A-8	11732422	20683730	15771281	412307

IV.   Case 1 - Grid Convergence Study

The first test case required for the workshop is a grid convergence study using the three successively refined grids for Configuration 1 described in the previous section. The test conditions for this case are specified as:

American Institute of Aeronautics and Astronautics

(a) Coarse   (b) Medium   (c) Fine
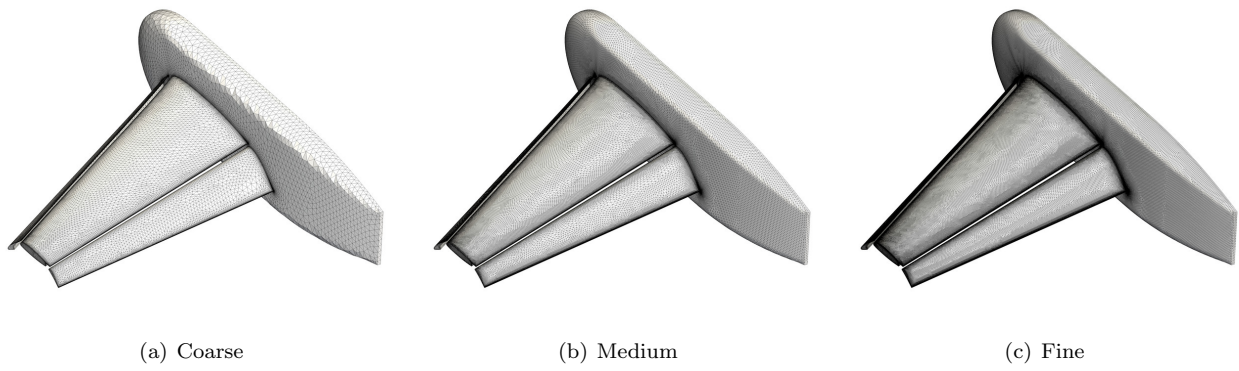
Figure 5. Overall grid resolution for Configuration 1

(a) Coarse   (b) Medium   (c) Fine
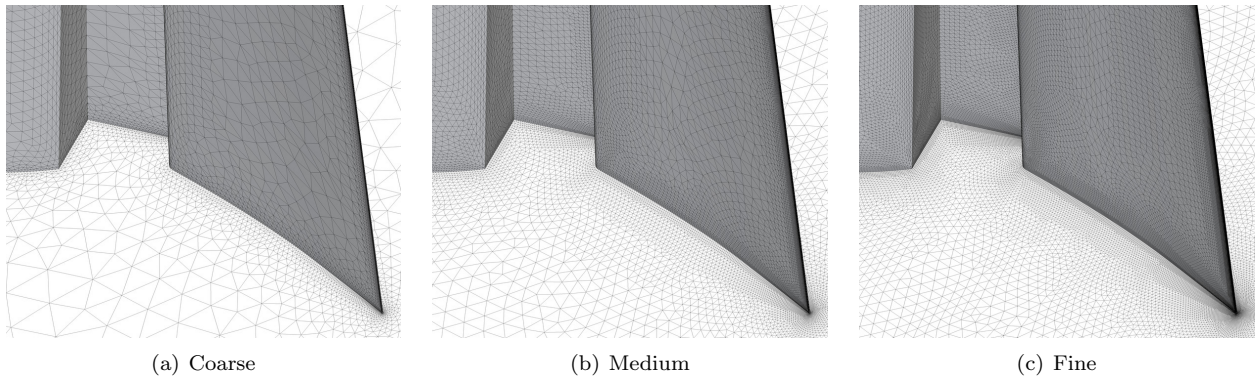
Figure 6. Flap cove grid resolution for Configuration 1

(a) Coarse   (b) Medium   (c) Fine
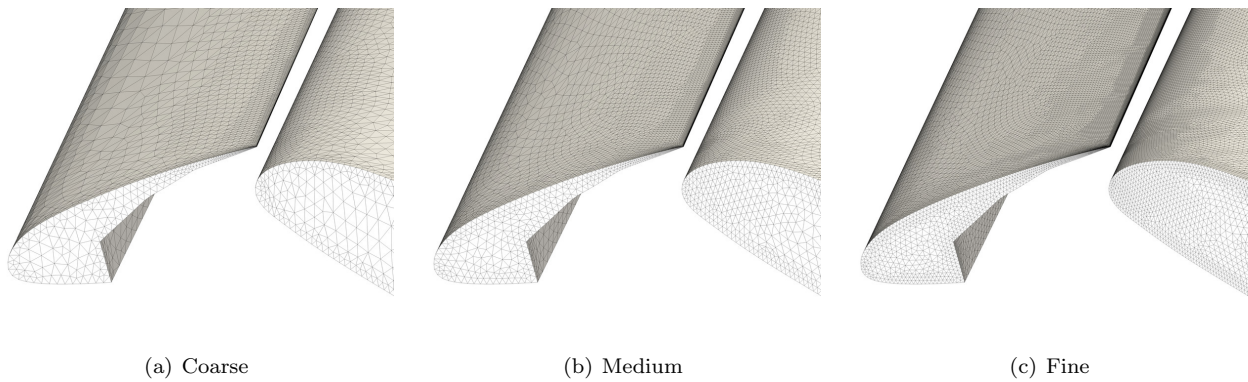
Figure 7. Slat outboard grid resolution for Configuration 1

American Institute of Aeronautics and Astronautics

- Mach Number = 0.2

- Angle-of-attack = 13° and 28°

- Reynolds Number = 4.3 million based on mean aerodynamic chord (MAC)

- Reference Temperature = 520R

The grid convergence plots are made versus the grid index, defined as the inverse of the number of grid points to the 2/3 power, with the understanding that for a family of self-similar coarse to fine grids, this quantity should be representative of the average cell size h to the second power. Thus, straight-line plots in these figures are indicative of second-order accurate spatial convergence and extrapolation to the y-axis provides an estimate of the values which would be predicted in the presence of infinite grid resolution.

Figure 8 shows the grid convergence behavior of the lift, drag and moment coefficients for the 13° case. For this case, the lift and moment coefficients both exhibit the desired linear convergence, while the drag value suggests a different infinite grid value between the coarse to medium and the medium to fine grids. It should be noted however that the magnitude of the drag variation is 0.5% while the variation is 2.1% in lift and 3.0% in the moment.

Figure 9 shows the grid convergence behavior for the 28° case. In this case the overall variation in lift and moment is similar to the previous case at 2.0% and 3.0%, respectively, while the variation in drag has increased to 1.4%. The plots also exhibit less linear behavior overall, suggesting that further grid refinement is needed to confidently identify the asymptotic grid convergence range at this angle of attack.

Although not required for the workshop, a complete alpha sweep (incidences = 6,13,21,28,32,34 and 37°) was carried out on all three grids for this configuration, in order to study the effect of grid resolution throughout the entire incidence range and near $C_{L_{max}}$. Figure 10 depicts the computed lift and drag and moment versus incidence curves along with the drag polar computed on all three grids. In general, minimal differences are observed in the linear portion of the lift slope curve, with the coarse grid slightly under-predicting the lift values, and slight over-prediction for the finest mesh. Larger grid sensitivity is seen near the $C_{L_{max}}$ region where the drag is also slightly overpredicted on all grids, possibly due to larger regions of separated flow in the simulations. The $C_{L_{max}}$ value and location are reasonably well predicted, although additional simulations at incidences near the $C_{L_{max}}$ point would be desirable to further quantify this important region. Compared to the force coefficients, the pitching moment values show greater sensitivity to grid resolution. Pitching moment magnitudes are generally underpredicted, although the shape of the curve is well predicted, and agreement with experiment improves with increasing grid refinement. Note that various modeling deficiencies such as the absence of the flap brackets in the CFD simulations may account for part of the discrepancies between the fine grid pitching moment results with experimental values.

V.   Case 2 - Flap Deflection Study

The second case for the workshop involves prediction of the effect of changing the flap angle on the aerodynamic forces and moments generated by the Trap Wing. The requirements for this case are as follows:

- "Config 1" - Slat 30°, Flap 25°

- "Config 8" - Slat 30°, Flap 20°

- Mach Number = 0.2

- AOA Values = 6,13,21,28,32,34 and 37°

- Reynolds number = 4.3 million based on MAC

- Reference Temperature = 520R

These simulations were done using the medium resolution grid on Configuration 1, and a grid of equivalent resolution (generated using the same parameters) on Configuration 8. Note that the medium grids for the workshop have been designed to be representative of current industrial production practice, and thus the current study is representative of the state-of-the-practice in prediction of design increments for high-lift configurations. Figures 11(a) through (c) depict the comparison of the computed lift and drag values versus

American Institute of Aeronautics and Astronautics

the wind tunnel data for the two flap positions. Both the lift and drag are close to the experimental data for both configurations for the majority of the alpha sweep, although experimental data was not available for Configuration 8 at the higher alpha values. At the onset of separation for Configuration 1, NSU3D accurately captures the declining lift curve slope, with the final lift and drag values being overpredicted at the highest angle where the flow exhibits significant separated regions. The same results are plotted in Figure 12(a) and (b) in terms of the percent change in lift and drag between these two configurations. Experimental increments are not available above 28 degrees, since there are no high incidence values for Configuration 8. The increments in lift and drag are reasonably well predicted in the linear region of the lift slope curve, although agreement with experiment degrades at the higher incidences.

Computed and experimental pitching moment coefficients for both configurations are compared in Figure 11(d) with the corresponding percent change values shown in Figure 12(c). In this case, the moment at $6°$ is predicted very accurately for both configurations. The increment between the two flap settings is also captured accurately at this incidence. Although the absolute moment values are not predicted as well as the force coefficient values throughout the incidence range, prediction of the increment in pitching moment between the two configurations is predicted well in the linear region of the lift slope curve, but degrades near the higher incidences in a similar manner to that observed for the force coefficient increments.

VI.   Comparison of Surface Pressures

Figures 13 through 16 show the pressures on four of the surface pressure tap rows available in the wind tunnel data along with the corresponding pressures predicted by NSU3D on the coarse, medium and fine grids. As can be seen in the figures the surface pressure is predicted accurately at the majority of the locations, with the medium and fine grids producing closer agreement than the coarse grid as expected. Agreement is good across the majority of the wing with significant deviation confined to approximately the outermost 10% of the span. As shown in the preceding sections, the the overall lift and drag predictions are very good at all but the highest angle-of-attack, suggesting that the differences in the predicted pressure on the outboard section has only a small impact on the forces. The influence on the predicted moment is more significant, however, where the wing sweep creates a larger moment arm at the outboard sections, resulting the underprediction of the magnitude of the moment. Discrepancies in outer span pressure values was also noted by a majority of workshop participants. Given the strong gradients at the wing tip due to vortex rollup, one may expect significant grid resolution sensitivity of the pressure values in this region. Surprisingly, the coarse grid results agree most closely with experimental values in these regions, although a more extensive grid refinement study would be required to establish the grid converged results in the wing tip region. Sensitivity to viscous term formulation and turbulence models is also a possible explanation for the variations in the outer span flow patterns, noting that the current results do not include the Navier-Stokes cross-diffusion terms and are confined to the Spalart-Allmaras turbulence model. Discrepancies in the flap upper surface pressures at the 50% span location for the higher incidences (i.e. Figures 14(d) and 15(d)) can be attributed to the omission of the flap brackets, since calculations by other workshop participants have shown that inclusion of the bracket geometry improves agreement in these regions on the flap at the higher incidences.[20]

VII.   Surface and Volume Flow Visualization

Figures 17 and 18 depicts the surface "oil flow" and volume streamlines, respectively, based on the solutions obtained on the medium resolution grid for Configuration 1. At low angle-of-attack, the flow is smooth across the entire wing with a region of trailing edge separation along a majority of the flap span, which decreases with increasing angle of attack. This flow pattern on the flap correlates with the pressure tap data, is consistent with other workshop simulations, and is qualitatively in agreement with the mini-tuft flow visualization pictures provided by the workshop committee from wind tunnel experiments.

As the incidence is increased, the flow first detaches from the outboard trailing edge of the main element, which pushes the flap stagnation line back to the trailing edge (Figure 17[c],[d],[e]). At the highest angle of $37°$, the flow has now separated from the outboard third of the slat, resulting in a significantly different flow field over the main element. The effective incidence of the flap is now also much lower as can be seen by the improved agreement in the pressure data with the experiment. These flow patterns are supported by the volume streamline visualization pictures shown in Figure 18.

American Institute of Aeronautics and Astronautics

Different surface flow patterns are seen near the wing tip as the incidence is increased, although the discrepancies in surface pressures in this region with experimental values calls into question the accuracy of the predicted wing tip flow patterns. Unfortunately, there are no experimental wind tunnel flow visualization data (mini-tuft or other) in this region for comparison.

VIII. Conclusions

A complete set of results for the first high lift prediction workshop has been reported using the NSU3D unstructured mesh Reynolds-averaged Navier-Stokes solver. All grids for the study were generated by the authors. These have been made available on the workshop web page and have been used by various other workshop participants. Results include a grid refinement study over the entire lift-slope curve, and a full angle-of-attack sweep for two flap positions. Comparison with experimental data shows good agreement, with deviation being greatest at the most outboard locations and higher incident angles.

Follow on studies are desirable to further investigate some of the effects and discrepancies noted in these calculations. These include:

- Simulations including the cross-derivative terms (full Navier-Stokes)

- Simulations using other turbulence models available within NSU3D.

- Modeling the slat and flap brackets

- Modeling the tunnel walls and comparing to uncorrected experimental data

- Time accurate simulations to better resolve the maximum lift region and post stall behavior.

IX. Acknowledgments

References

[1]Nash, S. M. and Rogers, S. E., "Numerical Study of a Trapezoidal Wing High-Lift Configuration," October 1997, SAE-1999-01-5559.

[2]Johnson, P. L., Jones, K. M., and Madson, M. D., "Experimental Investigation of a Simplified 3D High Lift Configuration in Support of CFD Validation," August 2000, AIAA-2000-4217.

[3]McGinley, C. B., Jenkins, L. N., Watson, R. D., and Bertelrud, A., "3-D High-Lift Flow Physics Experiment - Transition Measurements," June 2000, AIAA-2005-5148.

[4]Levy, D. W., Zickuhr, T., Vassberg, J., Agrawal, S., Wahls, R. A., Pirzadeh, S., and Hemsch, M. J., "Data Summary from the First AIAA Computational Fluid Dynamics Drag Prediction Workshop," *Journal of Aircraft*, Vol. 40, No. 5, 2003, pp. 875–882.

[5]Laflin, K., Klausmeyer, S. M., Zickuhr, T., Vassberg, J. C., Wahls, R. A., Morrison, J. H., Brodersen, O. P., Rakowitz, M. E., Tinoco, E. N., and Godard, J., "Data Summary from Second AIAA Computational Fluid Dynamics Drag Prediction Workshop," *Journal of Aircraft*, Vol. 42, No. 5, 2005, pp. 1165–1178.

[6]Vassberg, J. C., Tinoco, E. N., Mani, M., Brodersen, O. P., Eisfeld, B., Wahls, R. A., Morrison, J. H., Zickuhr, T., Laflin, K. R., and Mavriplis, D. J., "Abridged Summary of the Third AIAA Computational Fluid Dynamics Drag Prediction Workshop," *Journal of Aircraft*, Vol. 45, No. 3, 2008, pp. 781–798.

[7]Mavriplis, D. J. and Levy, D. W., "Transonic Drag Prediction using an Unstructured Multigrid Solver," *AIAA Journal of Aircraft*, Vol. 42, No. 4, 2003, pp. 887–893.

[8]Mavriplis, D. J., "Third Drag Prediction Workshop Results using the NSU3D Unstructured Mesh Solver," *AIAA Journal of Aircraft*, Vol. 45, No. 3, May 2008, pp. 750–761.

[9]Mavriplis, D. J. and Long, M., "NSU3D Results from the Fourth AIAA CFD Drag Prediction Workshop," AIAA Paper 2010-4364.

[10]Lee-Rausch, E. M., Buning, P. B., Mavriplis, D. J., Morrison, J. H., Park, M. A., Rivers, S. M., and Rumsey, C. L., "CFD Sensitivity Analysis of a Drag Prediction Workshop Wing/Body Transport Configuration," AIAA Paper 2003-3400.

[11]Lee-Rausch, E. M., Frink, N. T., Mavriplis, D. J., Rausch, R. D., and Milholen, W. E., "Transonic Drag Prediction on a DLR-F6 Transport Configuration using Unstructured Grid Solvers," *Computers and Fluids*, Vol. 38, No. 3, March 2009, pp. 511–532.

[12]Mavriplis, D. J., "Aerodynamic Drag Prediction Using Unstructured Mesh Solvers," *CFD-Based Drag Prediction and Reduction, eds. H. Deconoinck, K. Sermus and C. van Dam, VKI Lecture Series 2003-02, von Karman Institute for Fluid Dynamics, Rhode St-Genese, Belgium*, March 2003.

[13]Mavriplis, D. J., "Grid Resolution Study of a Drag Prediction Workshop Configuration Using the NSU3D Unstructured Mesh Solver," AIAA-Paper 2005-4729.

[14]Mavriplis, D. J. and Venkatakrishnan, V., "A Unified Multigrid Solver for the Navier-Stokes Equations on Mixed Element Meshes," *International Journal for Computational Fluid Dynamics*, Vol. 8, 1997, pp. 247–263.

[15]Spalart, P. R. and Allmaras, S. R., "A One-equation Turbulence Model for Aerodynamic Flows," *La Recherche Aérospatiale*, Vol. 1, 1994, pp. 5–21.

[16]Wilcox, D. C., "Re-assessment of the scale-determining equation for advanced turbulence models," *AIAA Journal*, Vol. 26, 1988, pp. 1414–1421.

[17]Menter, F. R., "Two-Equation Eddy-Viscosity Turbulence Models for Engineering Applications," *AIAA Journal*, Vol. 32, No. 8, 1994, pp. 1598–1605.

[18]Mavriplis, D. J., "Multigrid Strategies for Viscous Flow Solvers on Anisotropic Unstructured Meshes," *Journal of Computational Physics*, Vol. 145, No. 1, Sept. 1998, pp. 141–165.

[19]Mavriplis, D. J. and Pirzadeh, S., "Large-Scale Parallel Unstructured Mesh Computations for 3D High-Lift Analysis," *AIAA Journal of Aircraft*, Vol. 36, No. 6, Dec. 1999, pp. 987–998.

[20]Rumsey, C. R., Long, M., Stuever, R. A., and Wayman, T. R., "Summary of the First AIAA High-Lift Prediction Workshop," AIAA Paper 2011 to be presented at the 49th AIAA Aerospace Sciences Meeting, Orlando FL.

[21]Mavriplis, D. J., Aftosmis, M., and Berger, M., "High-Resolution Aerospace Applications using the NASA Columbia Supercomputer," *International Journal of High Performance Computing Applications*, Vol. 21, No. 1, 2007, pp. 106–126.

[22]"HLPW-1 Gridding Guidelines," http://hiliftpw.larc.nasa.gov/Workshop1/GriddingGuidelinesHiLiftPW1-11JUN09.pdf.

[23]Mavriplis, D. J., Vassberg, J. C., Tinoco, E. N., Mani, M., Brodersen, O. P., Eisfeld, B., Wahls, R. A., Morrison, J. H., Zickuhr, T., and Levy, D., "Grid Quality and Resolution Issues from the Drag Prediction Workshop Series," *Journal of Aircraft*, Vol. 46, No. 3, 2009, pp. 935–950.

[24]"HLPW-1 Workshop Submitted Grids," ftp://hiliftpw-ftp.larc.nasa.gov/outgoing/HiLiftPW1/OriginalGrids.
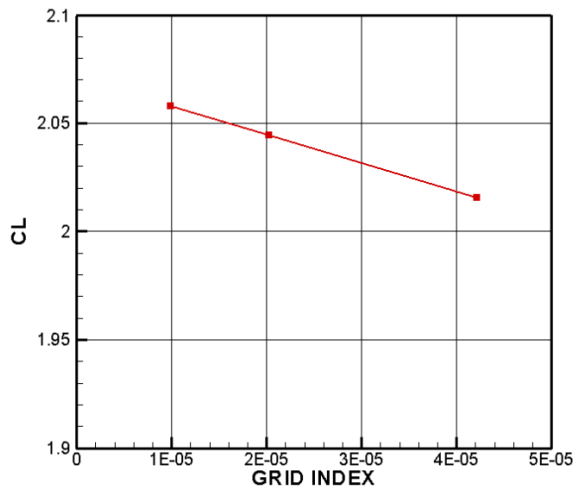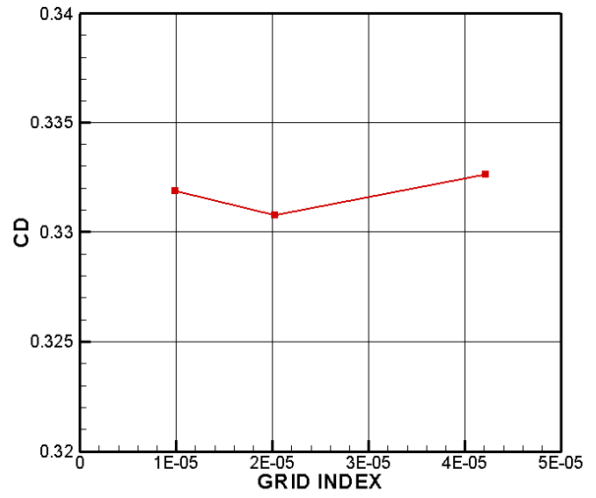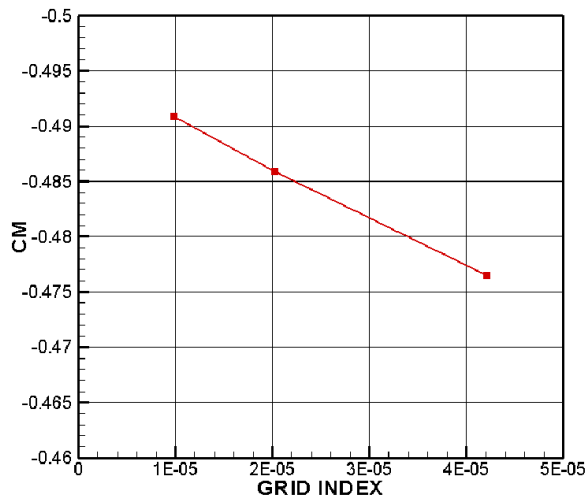
(a) Lift

(b) Drag

(c) Moment

Figure 8. Grid convergence plotted as variation in computed (a) lift (b) drag and (c) pitching moment coefficients versus the grid index defined as the number of grid points to the $2/3$ **power for Configuration 1 at an incidence of** $13°$

American Institute of Aeronautics and Astronautics
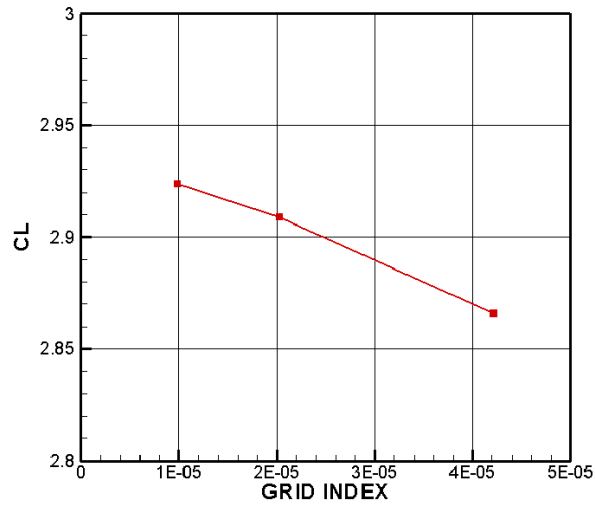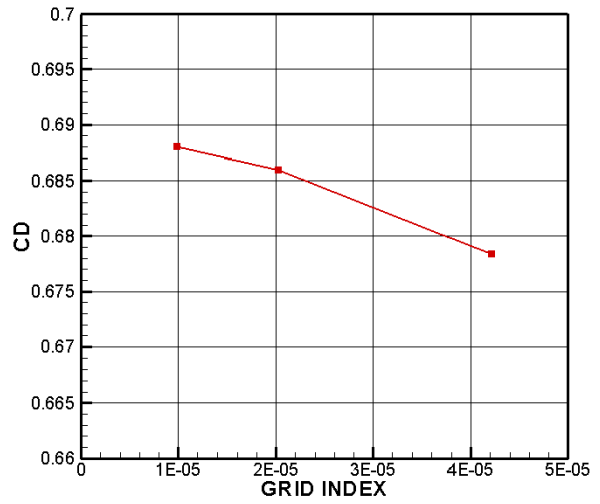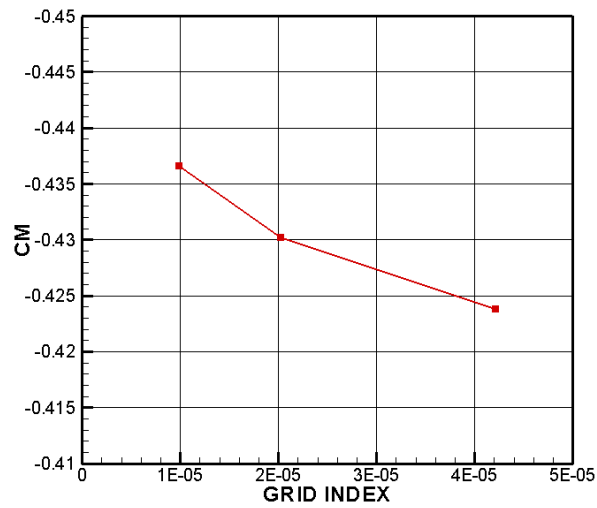
(a) Lift

(b) Drag

(c) Moment

Figure 9. Grid convergence plotted as variation in computed (a) lift (b) drag and (c) pitching moment coefficients versus the grid index defined as the number of grid points to the $2/3$ power for Configuration 1 at an incidence of $28°$
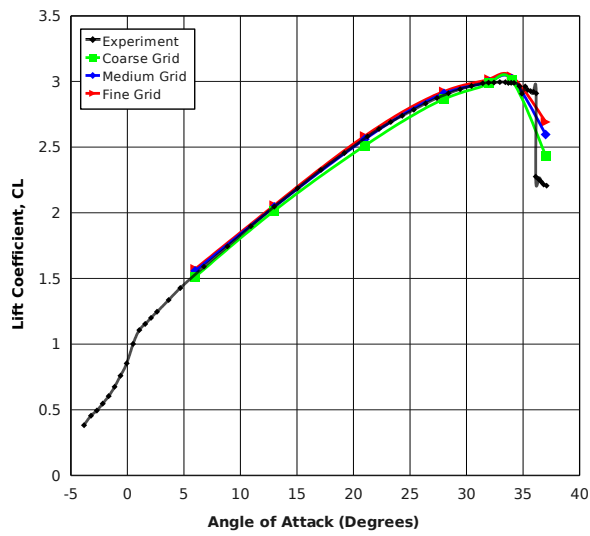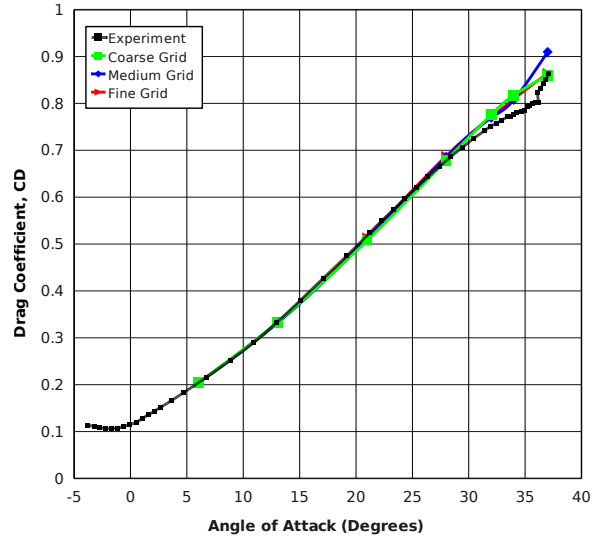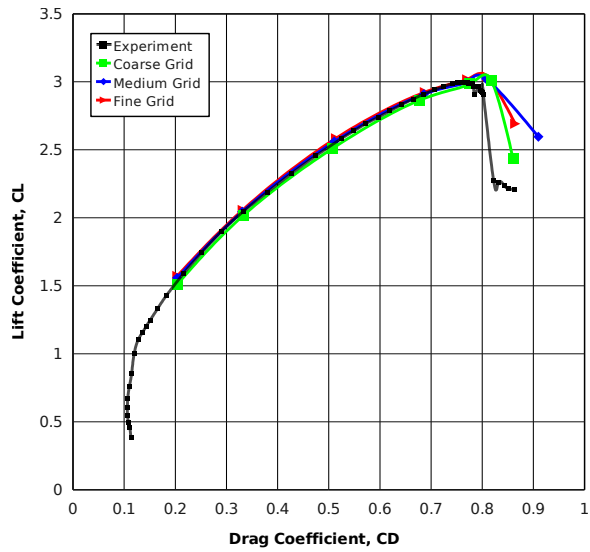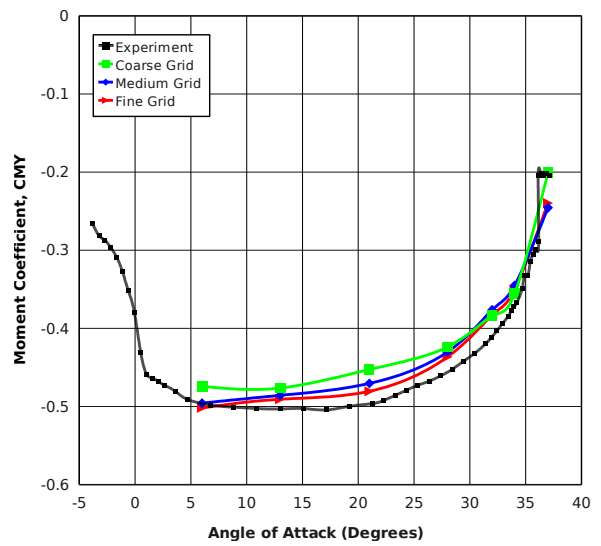
Figure 10. Computed forces on three different grid resolutions for Configuration 1 (a) Lift versus incidence, (b) Drag versus incidence, (c) Drag polar, (d) Pitching moment versus incidence

American Institute of Aeronautics and Astronautics
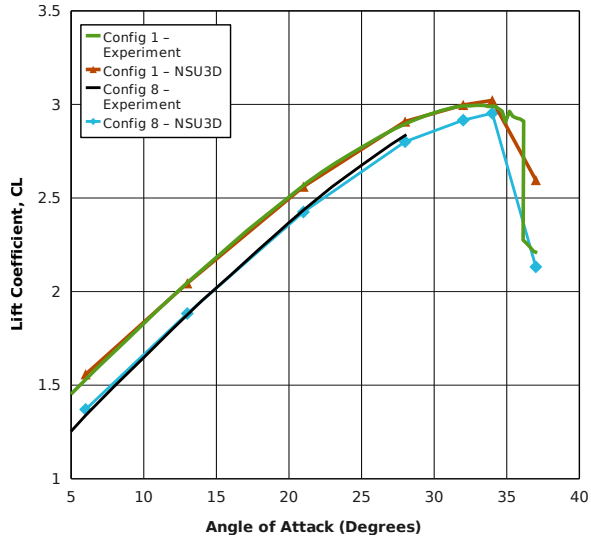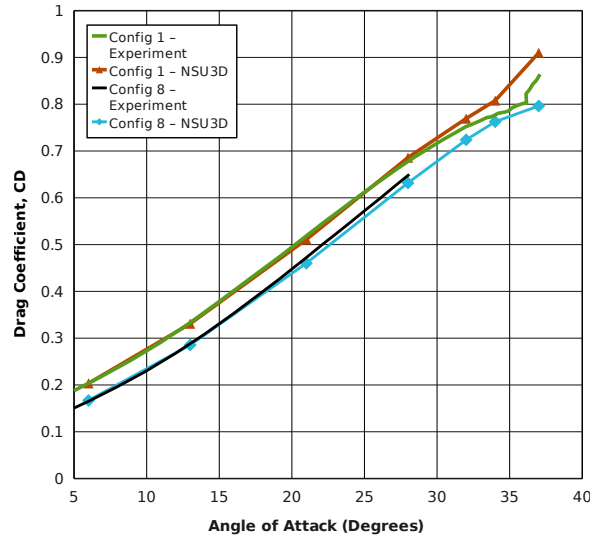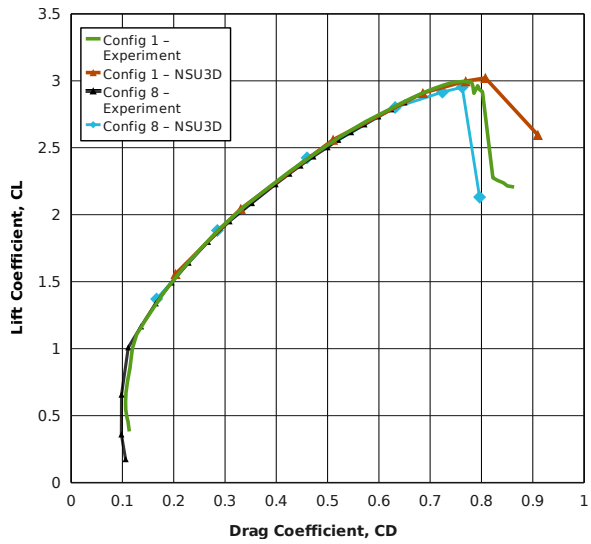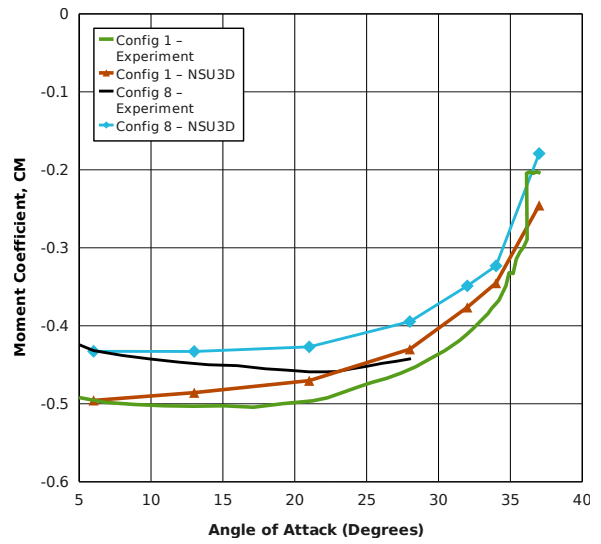
Figure 11. Computed and experimental results for flap deflection study (a) Lift versus incidence, (b) Drag versus incidence, (c) Drag Polar, (d) Pitching moment versus incidence

American Institute of Aeronautics and Astronautics
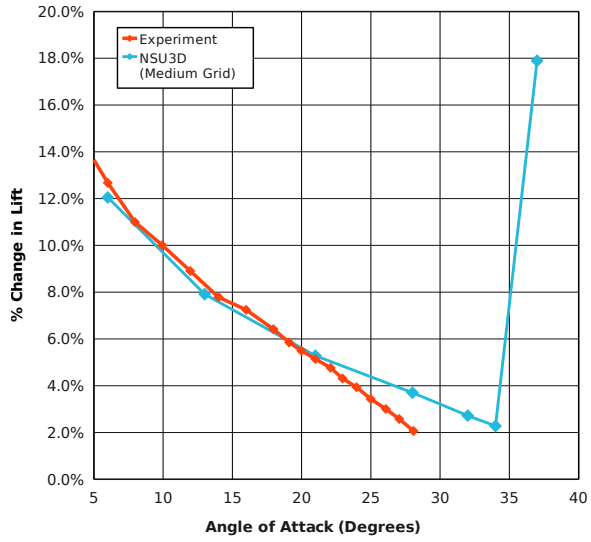
(a)
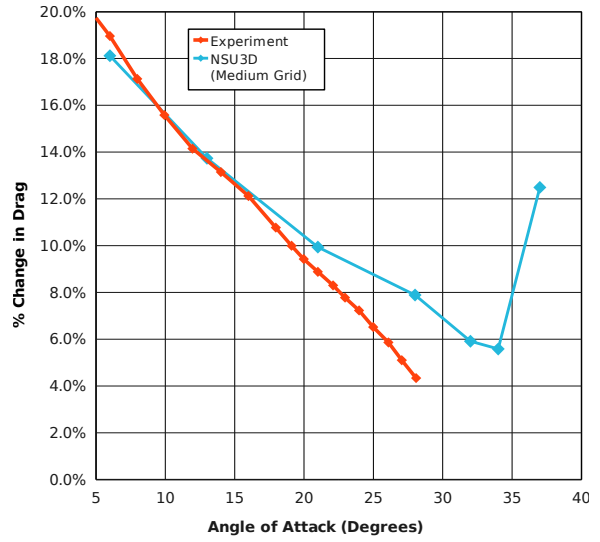
(b)
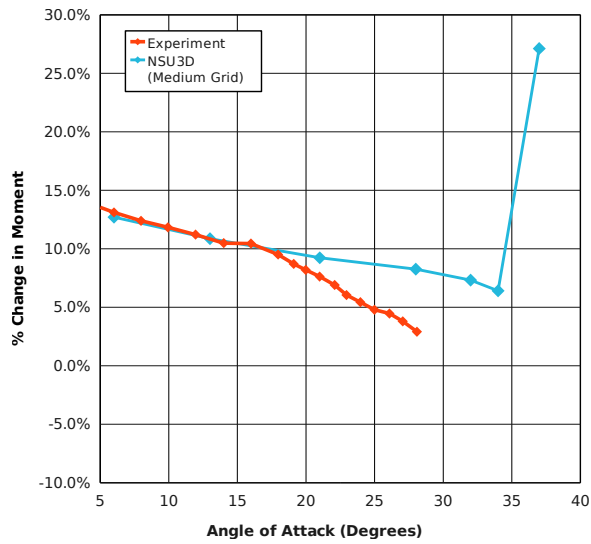
(c)

Figure 12.   Percent change in aerodynamic forces for flap deflection study (a) Lift, (b) Drag , (c) Pitching moment
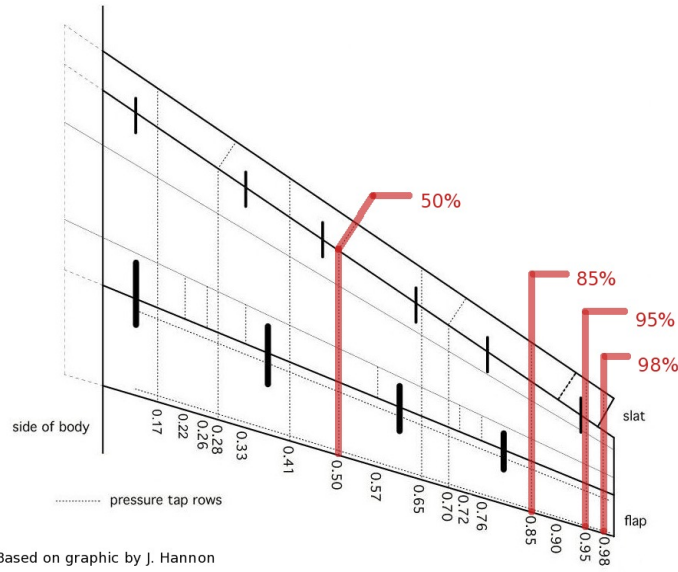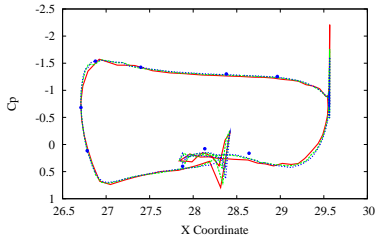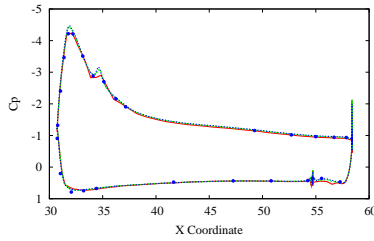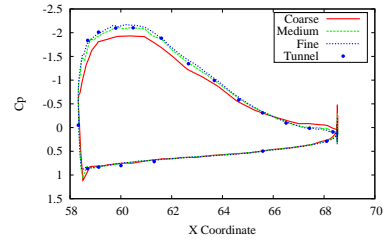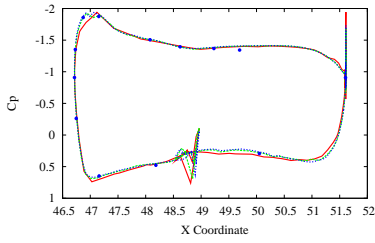
American Institute of Aeronautics and Astronautics
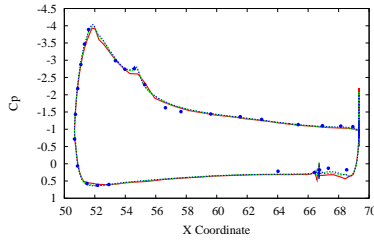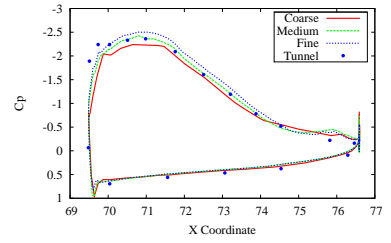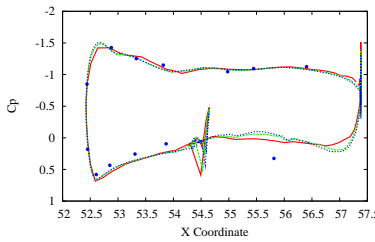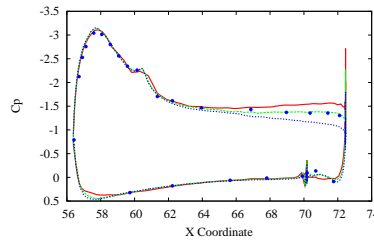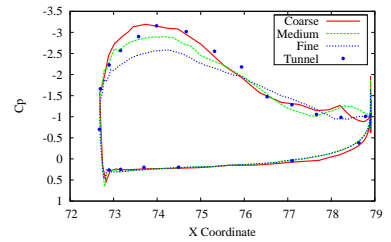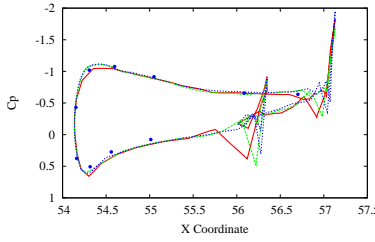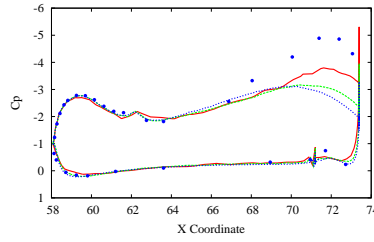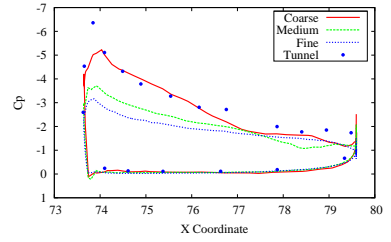
Figure 13. Comparison of computed surface pressures on three different grid resolutions with experimental data for Configuration 1 at $13°$ AOA
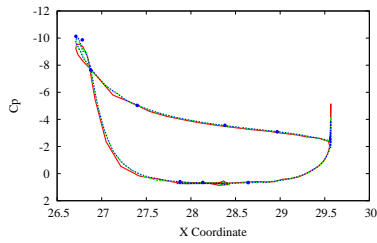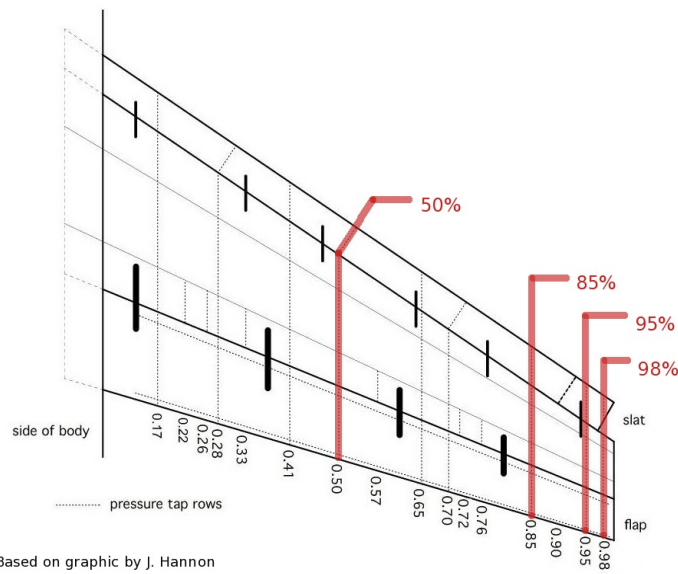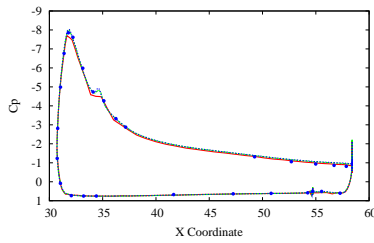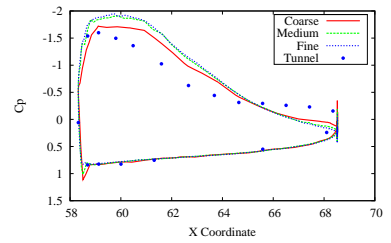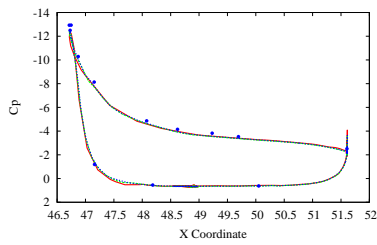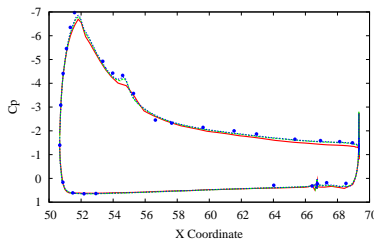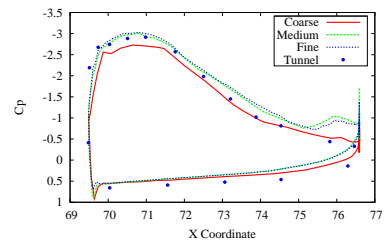
American Institute of Aeronautics and Astronautics
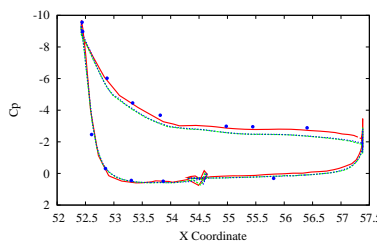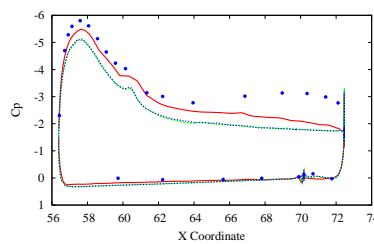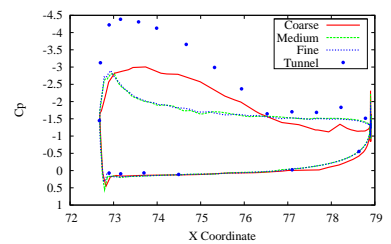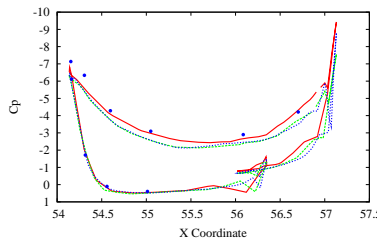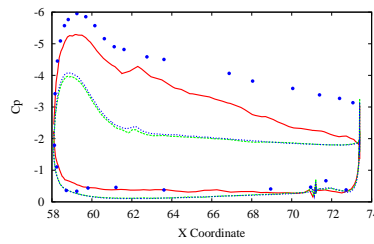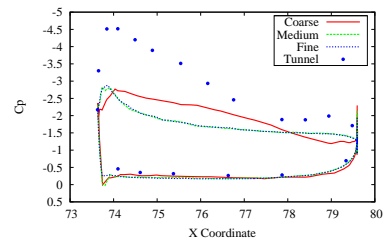
Figure 14. Comparison of computed surface pressures on three different grid resolutions with experimental data for Configuration 1 at $28°$ AOA
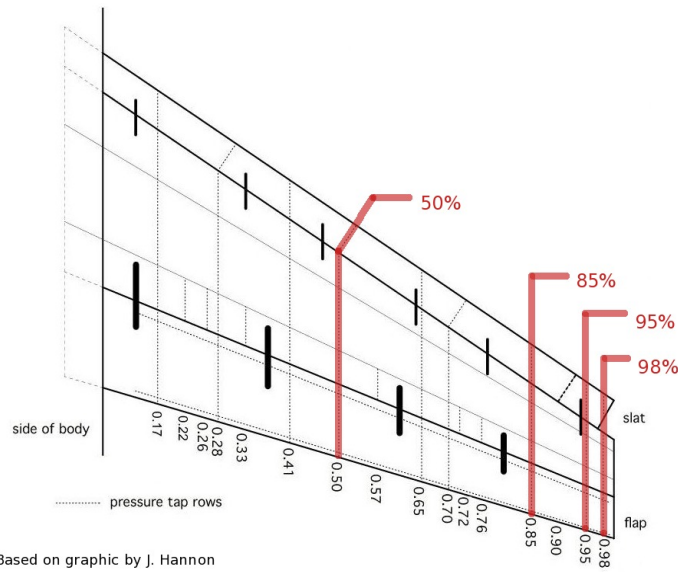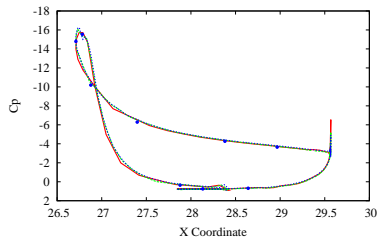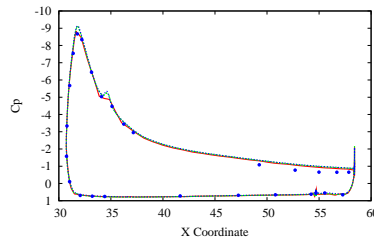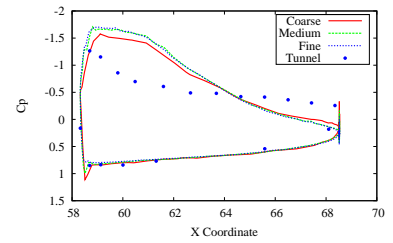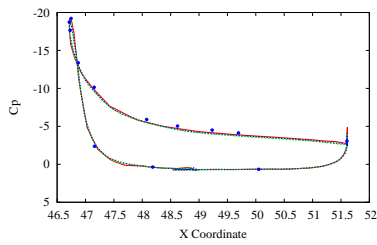
American Institute of Aeronautics and Astronautics

(b) Slat 50% Span

(c) Main 50% Span

(d) Flap 50% Span

(e) Slat 85% Span
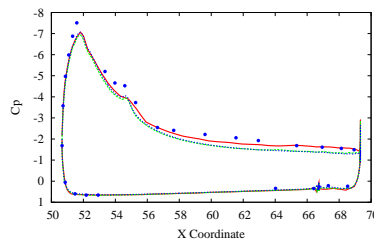
(f) Main 85% Span
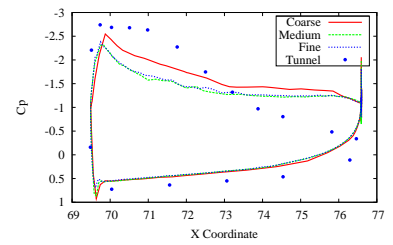
(g) Flap 85% Span
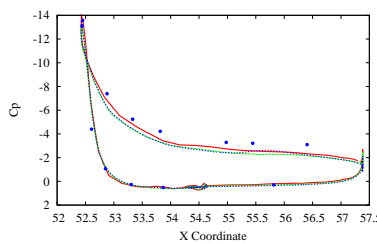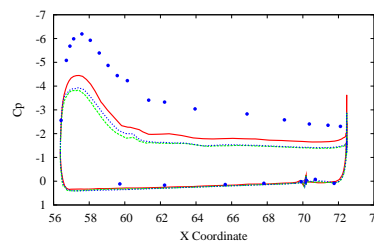
(h) Slat 95% Span
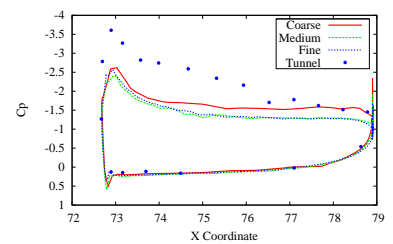
(i) Main 95% Span

(j) Flap 95% Span
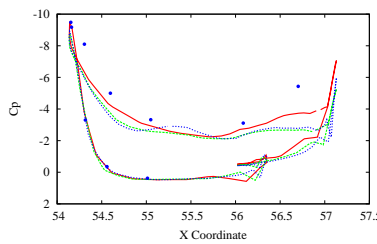
(k) Slat 98% Span
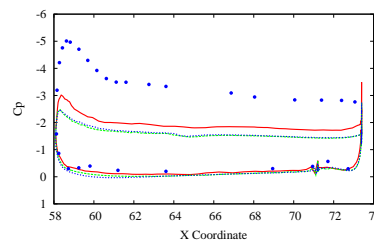
(l) Main 98% Span
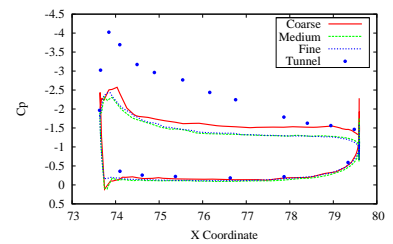
(m) Flap 98% Span

Figure 15. Comparison of computed surface pressures on three different grid resolutions with experimental data for Configuration 1 at $34°$ **AOA**
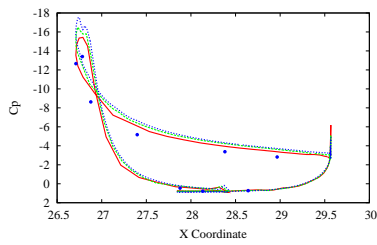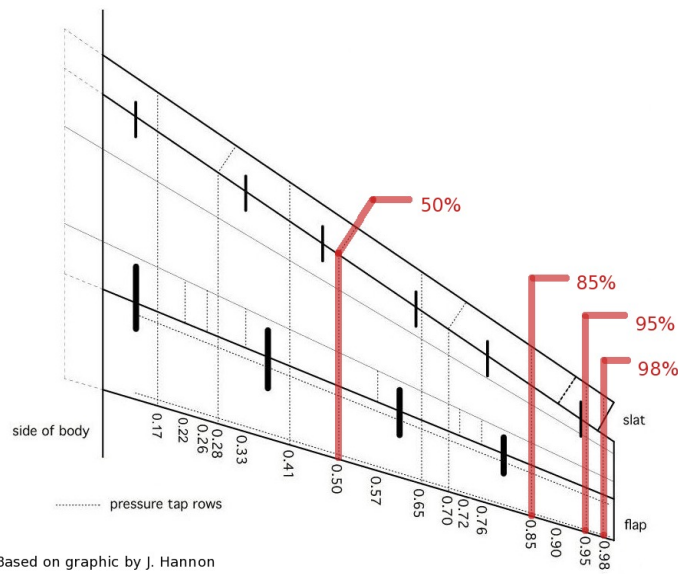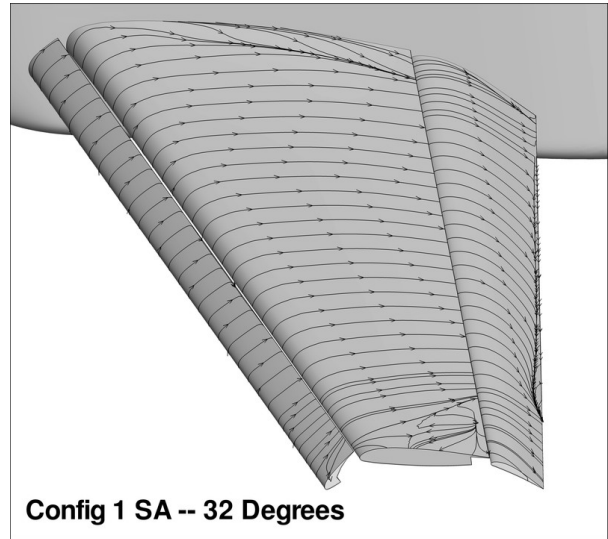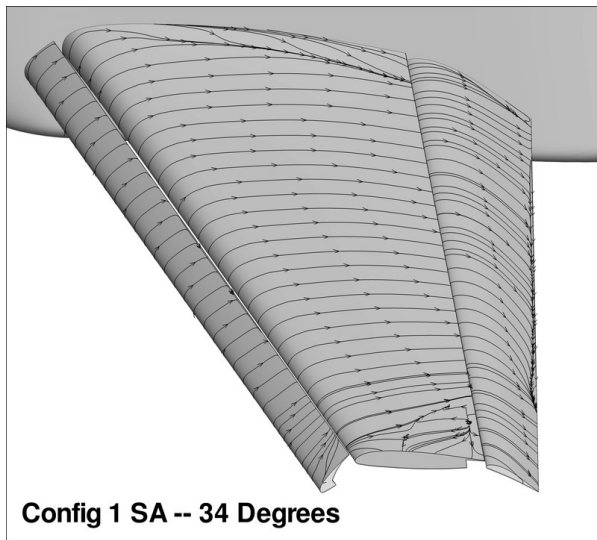
(b) Slat 50% Span
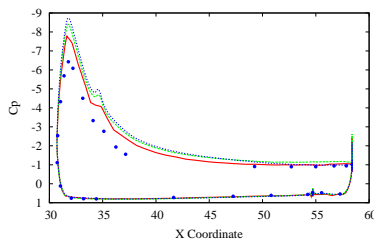
(c) Main 50% Span
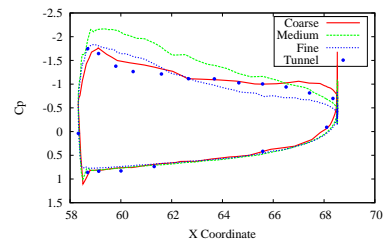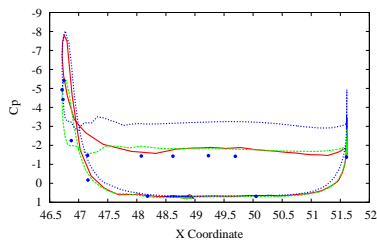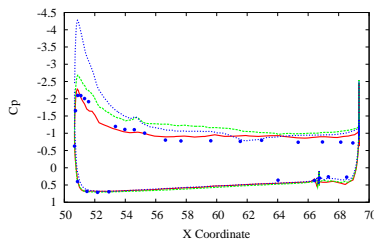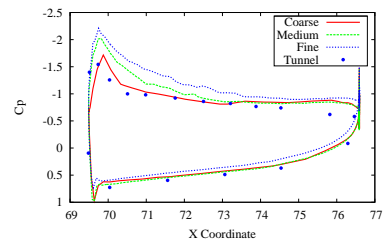
(d) Flap 50% Span

(e) Slat 85% Span

(f) Main 85% Span

(g) Flap 85% Span
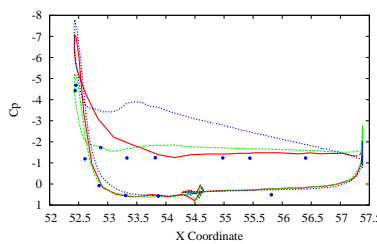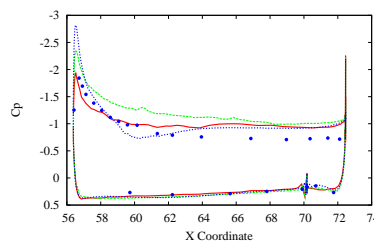
(h) Slat 95% Span
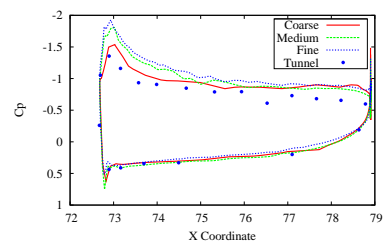
(i) Main 95% Span

(j) Flap 95% Span
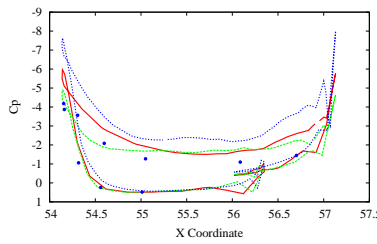
(k) Slat 98% Span
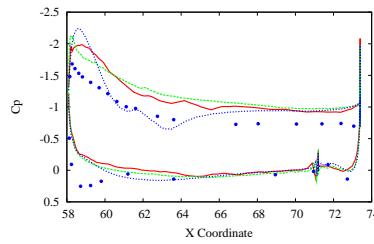
(l) Main 98% Span
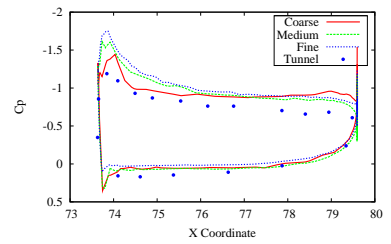
(m) Flap 98% Span

Figure 16. Comparison of computed surface pressures on three different grid resolutions with experimental data for Configuration 1 at $37°$ AOA

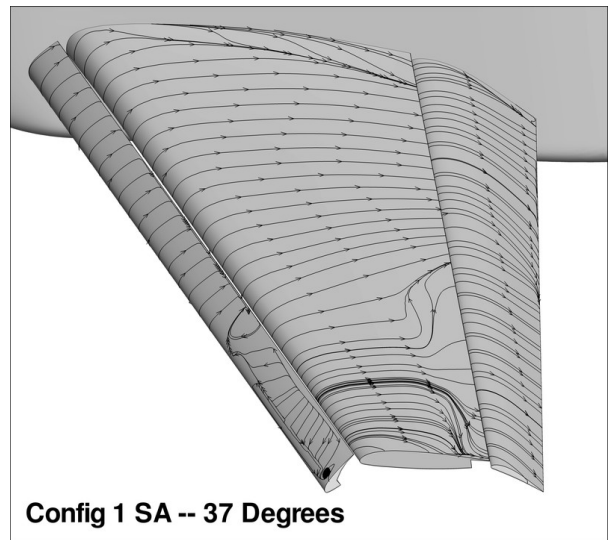American Institute of Aeronautics and Astronautics
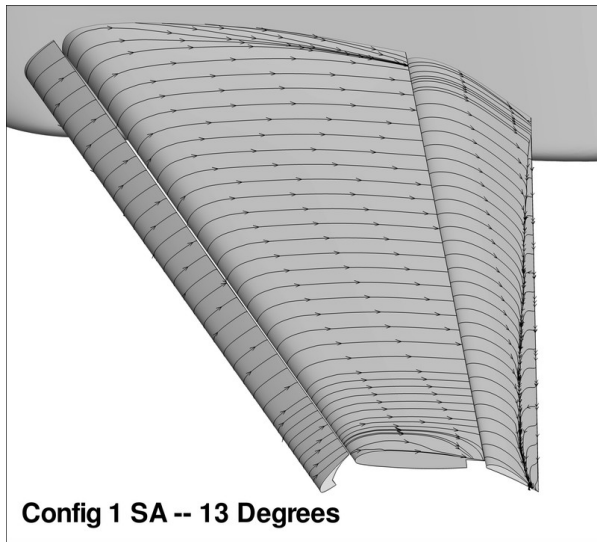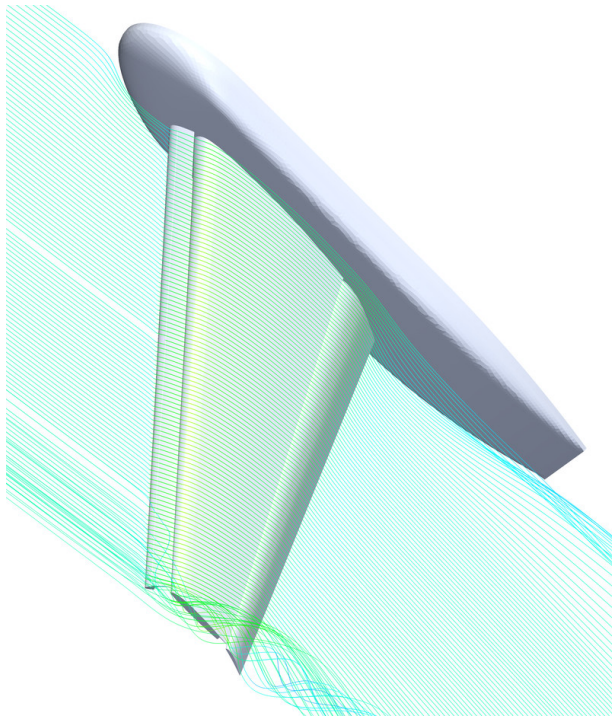
(a)
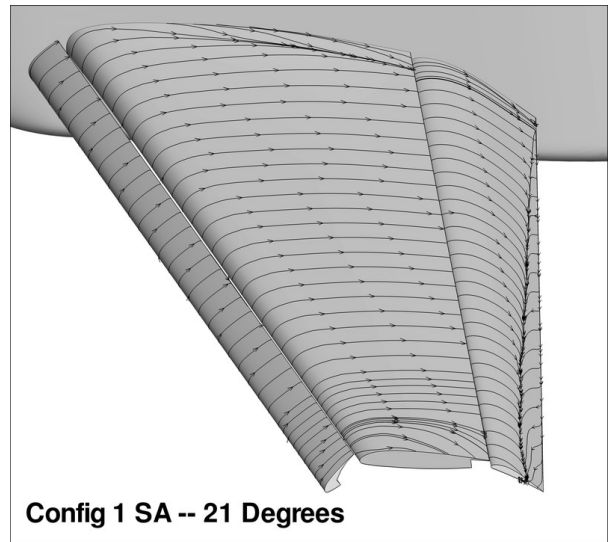
(b)
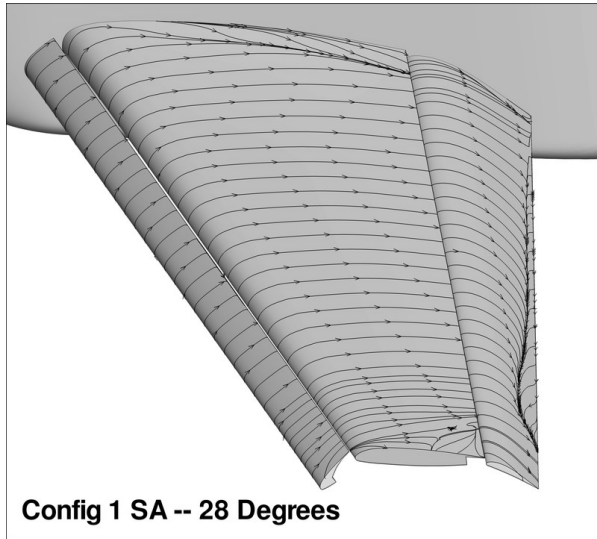
(c)

(d)

(e)

(f)

Figure 17. Surface flow visualization for Configuration 1 on medium grid at various incidences

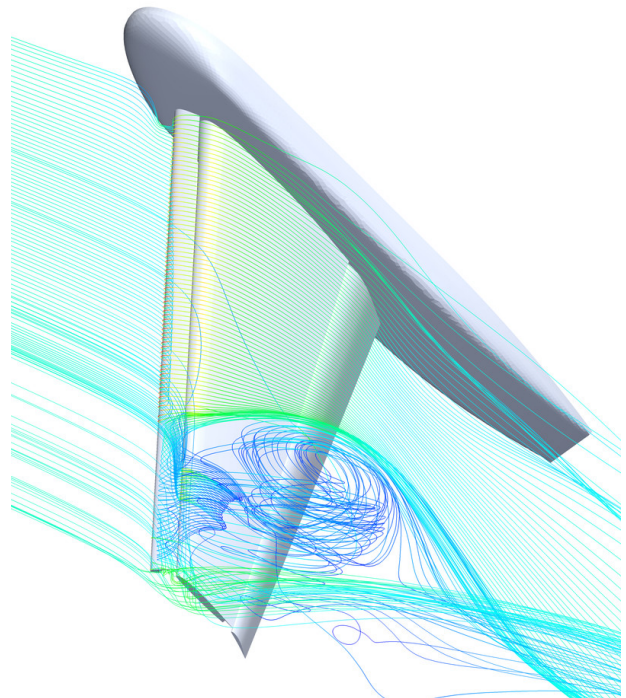American Institute of Aeronautics and Astronautics

(a) Alpha=13
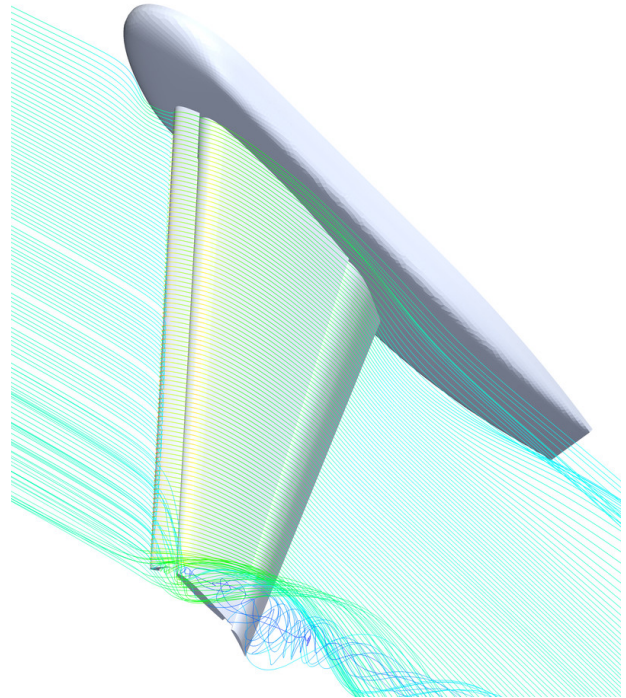
(b) Alpha=28
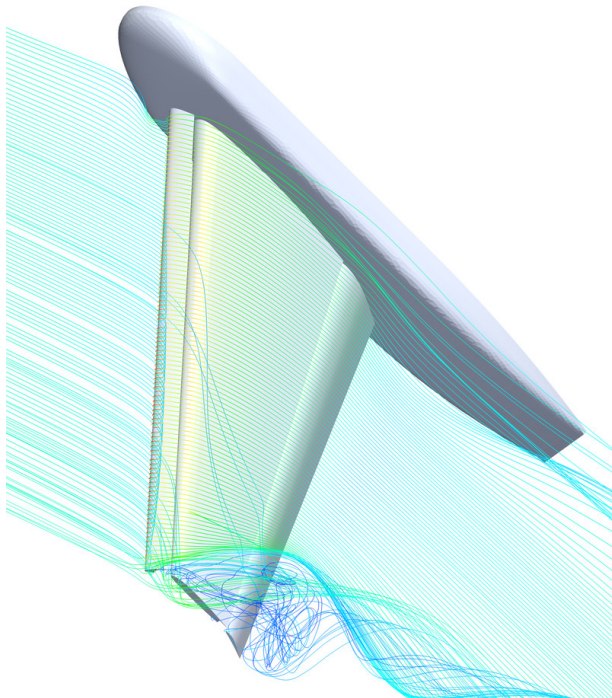
(c) Alpha=34

(d) Alpha=37

Figure 18. Volume flow visualization for Configuration 1 on medium grid at various incidences

American Institute of Aeronautics and Astronautics